Materials Today Communications xxx (xxxx) 102674

Contents lists available at ScienceDirect

Materials Today Communications

journal homepage: www.elsevier.com/locate/mtcomm

Developing an experimental-computational framework to investigate the deformation mechanisms and mechanical properties of Al-8Ce-10Mg alloys at micro and macroscales

Ryan J. Lane [a], Ayyoub M. Momen [b], Michael S. Kesler [c], Jamieson Brechtl [c], Orlando Rios [d], Kashif Nawaz [c], Reza Mirzaeifar [e, 1, *]

[a] Department of Biomedical Engineering and Mechanics, Virginia Tech, Blacksburg, VA 24061, United States
[b] Ultrasonic Technology Solutions, Knoxville, TN 37932, United States
[c] Oak Ridge National Laboratory, Oak Ridge, TN 37831, United States
[d] Department of Materials Science and Engineering, The University of Tennessee Knoxville, Knoxville, TN 37996, United States
[e] Department of Mechanical Engineering, Virginia Tech, Blacksburg, VA 24061, United States

ARTICLE INFO

Keywords:
Aluminum-cerium alloys (Al-Ce)
Crystal plasticity finite element modeling (CPFEM)
Microstructure
Scanning electron microscopy (SEM)

ABSTRACT

There is a promising future for the use of aluminum-cerium-magnesium alloys in a broad range of applications, including devices that operate at high temperatures. With cerium currently considered a waste product of rare earth mining validation studies of possible applications are essential to reduce the environmental waste. In this paper, a computational-experimental framework is developed to investigate the role both the intermetallic and matrix have on the mechanical properties of these alloys. A set of experiments, including SEM/EBSD imaging, nanoindentation, in-situ SEM tensile testing, and in-situ SEM-DIC tests are performed to characterize the microstructure and mechanical properties of these alloys. Furthermore, the elastic, plastic, and failure deformation mechanisms of the microstructure, and their correlation with the bulk scale mechanical properties are investigated. Experimental results are also used to calibrate parameters for a crystal plasticity finite element model, by performing a computational framework that minimizes the error between the computational and experimental results. This model is then utilized to investigate how the area percentage of intermetallics and the crystallographic texture control the mechanical properties of the alloy. Simulation results show that an increase in the percentage of intermetallics increase the strength but decrease the ductility of the alloy. Also, a change in material texture improves strength and reduces damage that leads to material failure. The development of the crystal plasticity model, as discussed in this work, opens opportunities for future investigations of similar aluminum-cerium-magnesium alloys.

1. Introduction

Cerium is currently categorized as a waste product in rare earth extraction with supply greatly out weighing demand [1]. More applications for the use of cerium are needed to lessen environmental impact and help stabilize the economics of rare earth extraction [1]. Rare earth minerals including cerium have been added to the critical mineral lists of The United States and European Union to ensure for sufficient supply for future private and militaristic needs indicating promising sustainability for rare earth alloys [2,3]. Recently, aluminum-cerium-magnesium alloys have shown great potential for use in casted heat exchanger applications [4,5].

The addition of Ce to Al alloys improves castability and creates a thermodynamically stable intermetallic upon solidification that maintains its structure up to the solidus temperature [4,6]. The added Mg greatly improves the yield strength of Al-Ce alloys and provides solid solution strengthening to the Al matrix without reacting with the Al-Ce intermetallic [4,7–9]. Al-Ce-Mg alloys form two main phases a Face Centered Cubic (FCC) Al(Mg) solid-solution and an Al-Ce intermetallic, $Al_{11}Ce_3$ [4,6,10].

* Corresponding author.
E-mail address: rmirzaei@vt.edu (R. Mirzaeifar).
[1] Lab URL: https://www.futurematerials-lab.com/.

https://doi.org/10.1016/j.mtcomm.2021.102674
Received 17 June 2021; Accepted 23 July 2021
2352-4928/© 2021

UNCORRECTED PROOF

A comprehensive review of the history of "Cerium in Aluminum Alloys" has been reviewed in [11] and studies composed of various material testing have been performed on different compositions of Al-Ce alloys to document different material characteristics. Tensile testing of various Al-Ce alloys reported bulk yield and ultimate stress properties [7]. Neutron diffraction measurements on Al-Ce alloys undergoing compressive loading observed bulk load sharing between the main phases of Al-Ce alloys [4,7]. Nanoindentation of the interface between two direct metal written paths of Al-Ce revealed a uniform modulus and local hardening suggesting effective load transfer at the interface [12]. Compression creep testing performed at elevated temperatures (greater than 260 °C) on Al-Ce alloys demonstrated loading sharing characteristics that aided in the alloys higher temperature strength [13]. Transmission Electron Microscopy investigating the orientation relationships between the $Al_{11}Ce_3$ intermetallic and Al matrix in the eutectic region reported partial coherency between the two phases at early phases of growth in the intermetallic [14]. However, to the best of our knowledge crystal plasticity finite element modeling (CPFEM) of Al-Ce-Mg alloys has not yet been reported.

The development of a crystal plasticity finite element model (CPFEM), with precisely calibrated parameters, will be essential to explicitly model all the microstructural features of the alloy. Crystal Plasticity modeling permits an accurate investigation of the elastic and plastic behavior at a microstructural scale for FCC materials [15]. While CPFEM has been used to investigate the effect of each phase on the mechanical behavior of materials at the micro- and macroscale levels for some multiphase materials [16–19]. The incorporation of crystal plasticity for metallic phases requires orientation dependent mechanical properties that normally consist of single crystal elastic constants, as well as plastic constants that govern slip dependent hardening equations [20]. The accuracy of the model is dependent on the calculation or calibration of these constants. For common alloys, the crystal plasticity constants are well documented and simply need to be input into a CPFEM, and any calibration of the parameters is performed using experimental data [21]. However, for a new multiphase alloy, these constants are unknown and need to be calculated or calibrated by various experimental techniques.

In this study, a crystal plasticity finite element model is developed for an Al-8Ce-10Mg (by nominal weight percent) alloy. The microstructure of a sample with a 52:1 extrusion ratio is considered, and a computational-experimental framework is developed for calibrating the crystal plasticity parameters. In this framework, scanning electron microscopy (SEM) and electron backscatter diffraction (EBSD) imaging are used to identify the microstructure and the texture. Nanoindentation and in-situ SEM tensile testing are utilized to characterize the elastoplastic mechanical properties, and the crystal plasticity parameters are calibrated by performing an optimization procedure to minimize the error between the computational results and the experimental characterizations. Lastly, the calibrated model is used to perform multiple simulations to investigate the effect of different properties and microstructure on the mechanical strength of the alloy.

2. Methods and materials

2.1. Crystal plasticity framework

In this work, we utilize a crystal plasticity framework that was developed into an Abaqus subroutine for a user defined mechanical material behavior (UMAT), to investigate the mechanical behavior of the Al (Mg) polycrystals subjected to uniaxial loading [20,22–27]. The crystal plasticity framework assumes that plastic deformation was caused by crystalline slip on a given slip system for FCC materials. The total deformation gradient, F, is defined as:

$$F = F^* \cdot F^P \tag{1}$$

where F^* is the strengthening and rotation of the lattice and F^P is the plastic shear of material compared to an intermediate reference configuration. The 12 slip systems are denoted by the symbol α, which is a combination of slip plane with a normal m_j^α and slip direction s_i^α. The velocity gradient of F^P is related to the slipping rate, $\dot{\gamma}^\alpha$, of the α slip system by:

$$L^P = \left[\dot{F}^P\right]\left[F^P\right]^{-1} = \sum_\alpha \dot{\gamma}^\alpha s_i^\alpha m_j^\alpha \tag{2}$$

The Schmid Stress, τ^α, is defined as the critical resolved shear stress when elastic lattice distortions are negligible, and is written as:

$$\tau^\alpha = s_i^\alpha \sigma_{ij} m_j^\alpha \tag{3}$$

The slipping rate ($\dot{\gamma}^\alpha$) in a rate dependent crystalline solid is in the form of a power law defined as:

$$\dot{\gamma}^\alpha = \dot{\gamma}_0^\alpha sign\left(\tau^\alpha\right)\left|\frac{\tau^\alpha}{g^\alpha}\right|^n \tag{4}$$

where, $\dot{\gamma}_o^\alpha$ is the reference slipping rate, $g^\alpha$is the current strength of the system, and n is the strain rate sensitivity ratio. When slip occurs, the Schmid Stress on any active slip system reaches the critical value g^α. On inactive slip systems with $\dot{\gamma}^\alpha = 0$, the Schmid Stress τ^α is less than g^α. The hardening law for the current strength is defined as:

$$\dot{g}^\alpha = \sum_\alpha h_{\alpha\beta}\dot{\gamma}^\beta \tag{5}$$

The slip hardening moduli $h_{\alpha\alpha}$ $(\alpha = \beta)$ and $h_{\alpha\beta}$ $(\alpha \neq \beta)$ are called the self-hardening and latent hardening moduli, respectively. The self-hardening moduli, which are not summed over in Eq. (6), are defined as:

$$h_{\alpha\alpha} = h(\gamma) = h_0 \mathrm{sech}^2\left|\frac{h_0\gamma}{\tau_s - \tau_0}\right| (\alpha = \beta) \tag{6}$$

When $\alpha \neq \beta$, the latent hardening moduli is defined by:

$$h_{\alpha\beta} = qh(\gamma)\ (\alpha \neq \beta) \tag{7}$$

where h_0 is the initial hardening modulus, τ_s is the saturation stress, τ_o is the initial stress, γ is the accumulated shear strain in the slip system, and q is the latent-hardening to self-hardening ratio. This crystal plasticity framework requires six parameters. The first three are the single crystal elastic constants $\left[C_{11}, C_{12}, C_{44}\right]$, while the other three are the plastic constants $\left[h_o, \tau_s, \tau_o\right]$. It is worth noting that these values are not available for the Al-Ce alloy. Therefore, the purpose of this work is to calibrate the parameters using experimental data obtained from EBSD, nanoindentation, and in-situ tensile testing, as will be discussed in the following sections.

2.2. Experimental procedures

All Al-8Ce-10Mg samples were extruded at a ratio of 52:1 [7]. The extrusion parameters were as followed. The billet and container busing were preheated to 420 °C. The compacting pressure was 10.13 MPa and remained constant throughout the process. The speed of the material outflow was between 3.5 and 4.0 m/min. A 1.25 in. diameter cylindrical billet was produced. The Al-Ce samples were EDM cut such that the loading direction was the same as the extrusion direction of the alloy. The samples were sectioned and polished down to EBSD requirements using 0.05 μm colloidal silica. Initial SEM backscatter imaging was done in a FEI Quanta 650 ESEM. An Al-Ce sample was etched with Keller's Reagent for 60 s and images of the grain boundaries in the alloy were captured. EBSD was performed on samples to calculate the average grain size and bulk microstructural texture. Scans were performed

UNCORRECTED PROOF

on samples in a JEOL JSM 6500 with an EDAX/EBSD detector. The scan area was 367 μm × 184 μm with a step size of 1 μm. The analysis of the EBSD data used a m-3m point group with Al lattice constants of 4.04 Å. The $Al_{11}Ce_3$ was not included in the list of phases and shows up as black in the EBSD scans for easy identification. The EBSD reconstructions were made using Dream3D software [28].

Nanoindentations were performed on the alloy using a Hysitron nanoindenter equipped with a Berkovich tip. Indents were conducted under load control with a loading rate of 1000 μN/s for 5 s, followed by a 2 s holding period at 5000 μN, and then unloading at the same rate. A 15 × 15 grid (225 points) with 10 μm spacing between points was performed on the sample to ensure that multiple grains and intermetallics were indented. Another EBSD scan of the microstructure was done on a 91 μm × 91 μm square portion of the grid with a step size of 0.4 μm. The EBSD results of the nanoindentation grid were used to determine the orientations of the grains that were indented.

A Kammrath & Weiss Tensile/Compression Module 5000 N load frame designed to be placed inside an SEM was used for in-situ tensile loading of rectangular dogbone specimens that were machined and polished. The gauge section of the dogbones was 23.5 mm in length with a cross sectional area of 10.5 mm^2 (3.5 mm × 3.0 mm) A 5000 N load cell with a precision of 0.1 N was installed in the frame for testing. The maximum stress that could be applied using a 5000 N load cell was 475 MPa, which was sufficient to cause failure in this Al-Ce alloy [29]. The tensile tests were performed in the FEI SEM in displacement control mode with a displacement rate of 2.35 μm/s. Backscatter SEM images were taken every 10 s during the tensile test.

To investigate the deformation mechanisms of the microstructure, particularly at the interface between the intermetallic and the matrix, additional in-situ SEM tensile tests were performed with a digital image correlation (DIC) pattern deposited on the surface of the sample. Gold nanoparticles with a size of 400 nm were chemically deposited onto the surface of the sample [30,31]. The tensile tests were performed in the FEI SEM in displacement control mode with the same displacement rate of 2.35 μm/s. SEM images were frequently collected at intervals of 50 N during the loading but stopped once the large intermetallic in the frame fractured. The SEM images were processed using Ncorr software [32] to produce the 2D strain distribution maps in the region of interest.

3. Results and discussion

3.1. Microstructural and crystallographic texture analysis

The backscatter SEM imaging of the Al-Ce alloy shows a clear distinction between the two main phases (Fig. 1(a)). The darker gray areas correspond to the Al(Mg) grains while the white rectangular areas represent the Al-Ce intermetallic phases. The extrusion direction of the alloy, indicated by the white arrow in Fig. 1(a), is parallel to the vertical axis in the image. The extrusion of the alloy creates lines of the intermetallics that are also parallel to the extrusion direction. The sample etched with Keller's Reagent (Fig. 1(b)) reveals the grain boundaries of the Al(Mg) phase.

An image of the EBSD reconstruction is shown in Fig. 2(a). The extrusion direction of the alloy was in the vertical direction of the reconstruction. Analysis of the EBSD results showed that the average grain size of the Al(Mg) grains was 13.5 μm ± 3 μm. Plotting the inverse pole figures, as shown in Fig. 2(b), reveals that the alloy has a slight [110] texture, which refers to the case that <110> crystal orientations are aligned, in loading and extrusion direction. The EBSD data was used to create finite element models that will be presented in Sections 3.4–3.6.

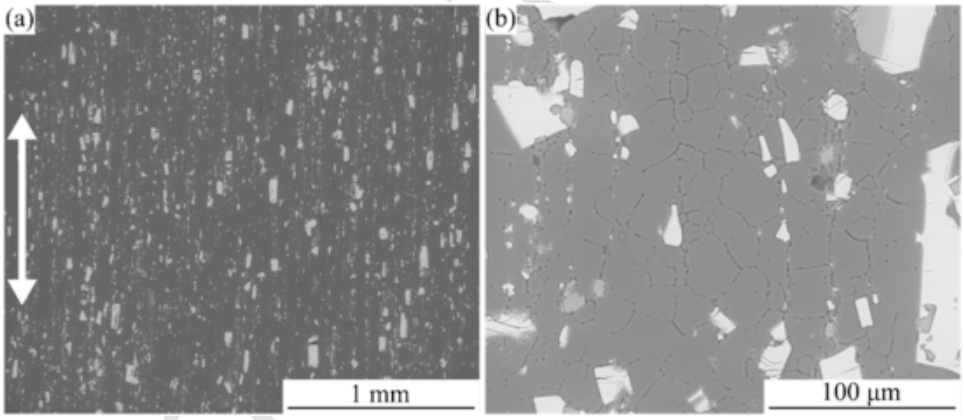

Fig. 1. (a) SEM backscatter image of the Al-8Ce-10Mg 52:1 microstructure with the gray area indicating Al(Mg) matrix and the white areas represent individual Al-Ce intermetallics. (b) SEM backscatter of the same microstructure that was etched with Keller's Reagent to reveal the grain boundaries in the Al(Mg) matrix.

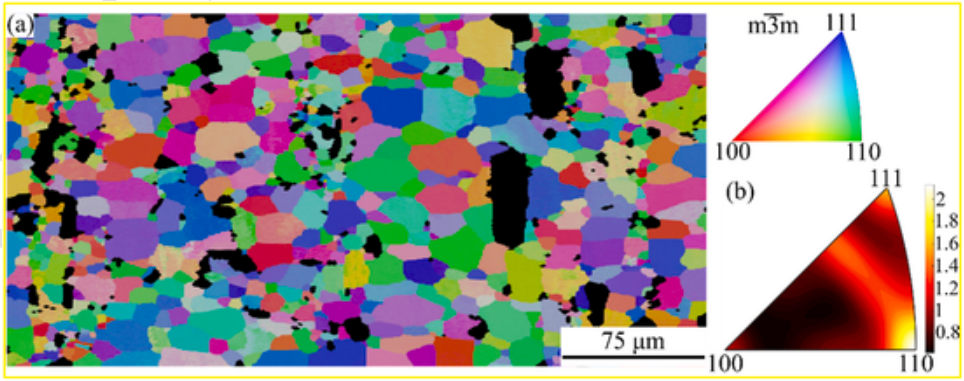

Fig. 2. (a) EBSD reconstruction of scans done on the Al-8Ce-10Mg 52:1 microstructure with the extrusion direction in the vertical direction. (b) The inverse pole figure of EBSD scan done on Al-8Ce-10Mg 52:1 microstructure with a microstructural texture in the [110] direction.

3.2. Single crystal elastic constant calculation using nanoindentation

An area of the surface was selected and nanoindentation was performed on a 15 × 15 grid. An EBSD scan was performed on a portion of the nanoindentation grid, as shown in Fig. 3(a). The purpose of the EBSD scan was to detect the crystal orientations of the grains corresponding to each of the points in which the nanoindentation was performed. The EBSD results indicate that multiple intermetallics were indented as well as multiple grain orientations. The load versus displacement curves for the indents performed on an intermetallic and grain are shown in Fig. 3(b) and circled in Fig. 3(a). The maximum displacement for the intermetallic is slightly less than 200 nm, as compared to ~ 400 nm for the grains. The overall shape of the curves was different for the intermetallic, where the sample exhibited more elastic recovery during unloading. Comparing the hardness values that were calculated from the test results, the intermetallic averaged 5.59 GPa with a standard deviation of 1.02 GPa while the grains averaged 1.37 GPa with a standard deviation of 0.07 GPa.

The nanoindentation data was used to calculate the single crystal elastic constants C_{11},C_{12}, and C_{44} using a process developed by Pierce [33–35]. To calculate the stiffness values, the slope during elastic recovery for grain orientations in the [100], [110], [111], and the Young's modulus, as calculated from nanoindentation using Eq. (8), were used [36]. The Young's modulus of the grains was calculated using the Reduced Modulus, E_r (74.46 GPa), the Poisson ratio of the grains of 0.3, and Young's modulus, E_i (1140 GPa), and Poisson ratio,v_i (0.07), for the Diamond Berkovich indenter.

$$\frac{1}{E_r} = \frac{1-\nu^2}{E} + \frac{1-\nu_i^2}{E_i} \tag{8}$$

The EBSD scan of the nano grid shows multiple indents on grains with orientations in the [100], [110], and [111] directions. The slope of the unloading curve, dP/dh, at the maximum depth of the load versus displacement curve, can be calculated using the Oliver–Pharr method [36]:

$$S = \frac{dP}{dh} = \frac{2\sqrt{A}}{\sqrt{\pi}} M_r \tag{9}$$

where S is the slope of the unloading curve, A is the contact area, and M_r is the reduced modulus. The reduced modulus is related to an orientation dependent indentation modulus, $M_{(hkl)}$, for elastically anisotropic materials using an axisymmetric indenter (such as the Berkovich indenter used in this study) by [34,37]:

$$\frac{1}{M_r} = \left(\frac{1}{M_{(hkl)}}\right) + \left(\frac{1-\nu_i^2}{E_i}\right) \tag{10}$$

An average $M_{(hkl)}$ value was calculated from multiple indentation results for grain orientations in the [100], [110], and [111] directions and were 81.79, 80.08, and 81.40 GPa, respectively.

The orientation dependent indentation modulus is related to the single crystal elastic constants C_{11}, C_{12}, and C_{44} [34]. The $M_{(hkl)}$ values for three different orientations are combined with methods developed by Vlassak and Nix (VN) and Hersey–Kroner–Eshelby (HKE) to calculate the single crystal constants [34,37,38]. The HKE method consists of a cubic equation for the bulk shear modulus, G, as a function of the single crystal elastic constants in the form:

$$G^3 + \alpha G^2 + \beta G + \gamma = 0,$$
$$\alpha = \frac{5C_{11}+4C_{12}}{8} \quad \beta = -\frac{C_{44}(7C_{11}-4C_{12})}{8} \quad \gamma = -\frac{C_{44}(C_{11}-C_{12})(C_{11}+2C_{12})}{8} \tag{11}$$

The VN method relates the orientation dependent indentation modulus to the polycrystalline indentation modulus, $\frac{E}{1-\nu^2}$, by a correction factor $\beta_{(hkl)}$. Here, $M_{(hkl)}$ and $\beta_{(hkl)}$ are related to the Young's modulus (E) and Poisson ratio (ν) of the polycrystalline material by:

$$M_{(hkl)} = \beta_{(hkl)}\left(\frac{E}{1-\nu^2}\right),$$
$$\beta_{(hkl)} = a + \nu\left(A - A_0\right)^B \tag{12}$$

The correction factor values for a, A_0, and B were calculated in a study done by Vlassak and Nix [34]. The values are dependent on the crystal orientation of the grain. The value of Poisson ratio was assumed to be 0.3 and the values for a, A_0, and B where input for orientations in the [111] and [100] directions. A ratio was taken using Eq. (13), that was based on the experimental values of the orientation dependent indentation modulus for the [111] and [100] directions, to form an equation for the anisotropy ratio $A_{(hkl)}$:

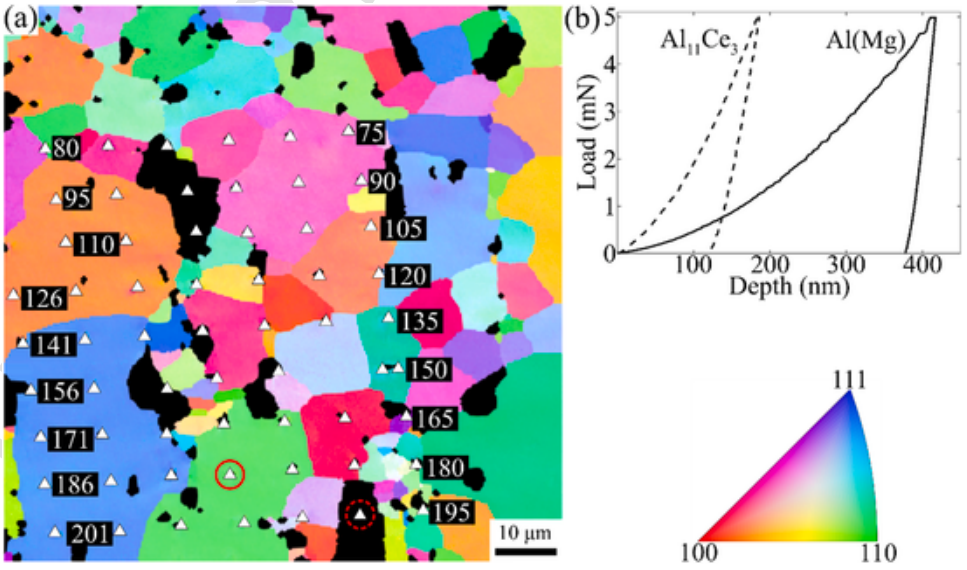

Fig. 3. (a) EBSD scan reconstruction of the partial nanoindentation grid. The nanoindentation points are marked according to their respective indentation number in the grid. The red circles correspond to their plotted load-displacement curves. (b) Plotted load versus displacement curves for the nanoindentations that were performed on the Al(Mg) grain (solid line) and Al-Ce intermetallic (dashed line).

UNCORRECTED PROOF

$$\frac{M_{(111)}}{M_{(100)}} = \frac{a_{111} + v_{111}\left(A_{111} - A_{0,111}\right)^{B_{111}}}{a_{100} + v_{100}\left(A_{100} - A_{0,100}\right)^{B_{100}}} \tag{13}$$

The single crystal elastic constants are related to the anisotropy ratio by [35]:

$$A = \frac{2C_{44}}{C_{11} - 2C_{12}} \tag{14}$$

The polycrystalline indentation modulus was calculated by using the experimental data for the [100] and [111] directions using Eq. (15).

$$\frac{1}{2}\left(\frac{M_{(111)}}{\beta_{(111)}} + \frac{M_{(100)}}{\beta_{(100)}}\right) = \left(\frac{E}{1 - \nu^2}\right) \tag{15}$$

The polycrystalline Poisson ratio was then calculated from the indentation modulus using Eq. (15) and the Young's modulus determined from Eq. (8). The bulk modulus, K, was calculated using the Young's modulus and Poisson ratio, and is related to single crystal elastic constants by:

$$K = \frac{E}{3\left(1 - 2\nu\right)} = \frac{C_{11} + 2C_{12}}{3} \tag{16}$$

The polycrystalline and single crystal bulk moduli are assumed to be equal [38]. The shear modulus was calculated using the Young's modulus and Poisson ratio by the classical equation:

$$G = \frac{E}{2\left(1 + \nu\right)} \tag{17}$$

The shear modulus that was calculated using Eq. (17) was plugged into Eq. (11), and a system of equations using Eqs. (11), (14), and (16) determined was solved for the single crystal elastic constants. Eq. (11) produces two sets of solutions for the constants. However, due to elastic stability, one of the sets can be removed [33]. The values found for the single crystal elastic constants for Al-8Ce-10Mg 52:1 are shown in Table 1. The values used in the crystal plasticity modeling presented in this study are in good agreement with the elastic slopes from the experimental data.

Table 1
Single crystal elastic constants for Al-8Ce-10Mg 52:1 calculated using nanoindentation data.

C_{11} (GPa)	C_{12} (GPa)	C_{44} (GPa)	E (GPa)	ν	G (GPa)	K (GPa)
100.41	42.59	28.31	74.46	0.3	28.56	61.88

3.3. In-situ SEM tensile testing

In-situ SEM tensile testing was performed to collect imaging data of the mechanical behavior of microstructure during loading. A total of 137 images were captured from start to failure of the specimen. After an elapsed time of approximately 23 min, the specimen broke near the middle of the gauge section. Fig. 4(a) displays the state of the microstructure at various strain points during the test where loading occurred in the direction of the white arrow. Imaging results indicate that the Al-Ce intermetallic forms microcracks perpendicular to the loading direction at around 2.5% bulk strain. The number of cracks in the intermetallic increases as the bulk strain of the material increases during testing.

The stress-strain curve of the test is plotted in Fig. 4(b). A dashed line is plotted for the Young's modulus of the material and the plastic response of the tensile test is adjusted to that line for calculating strain. The yield stress of the material was 149 MPa and the ultimate stress was 304 MPa. The in-situ tensile results were similar to those from tensile tests performed in other studies on the same alloy [29]. The total strain at failure was 16.67%, and failure occurred (with no signs of necking) shortly after the ultimate stress was reached.

The formation of the microcracks due to the brittle mechanical behavior of the intermetallics was a key failure mechanism for the material. Secondary SEM images were taken of the fracture surface after the completion of the tensile testing (Fig. 4(c)). The dimpling patterns in the Al(Mg) phase and clean fracture surfaces of the Al-Ce phases indicate that the failure mechanism for this Al-Ce alloy is ductile failure by microvoid coalescence. Similar phenomena have been observed in other Al intermetallic alloys [4,19,39–41]. Here, increasing displacement is accompanied by greater microcrack creation (Fig. 4(a)). As

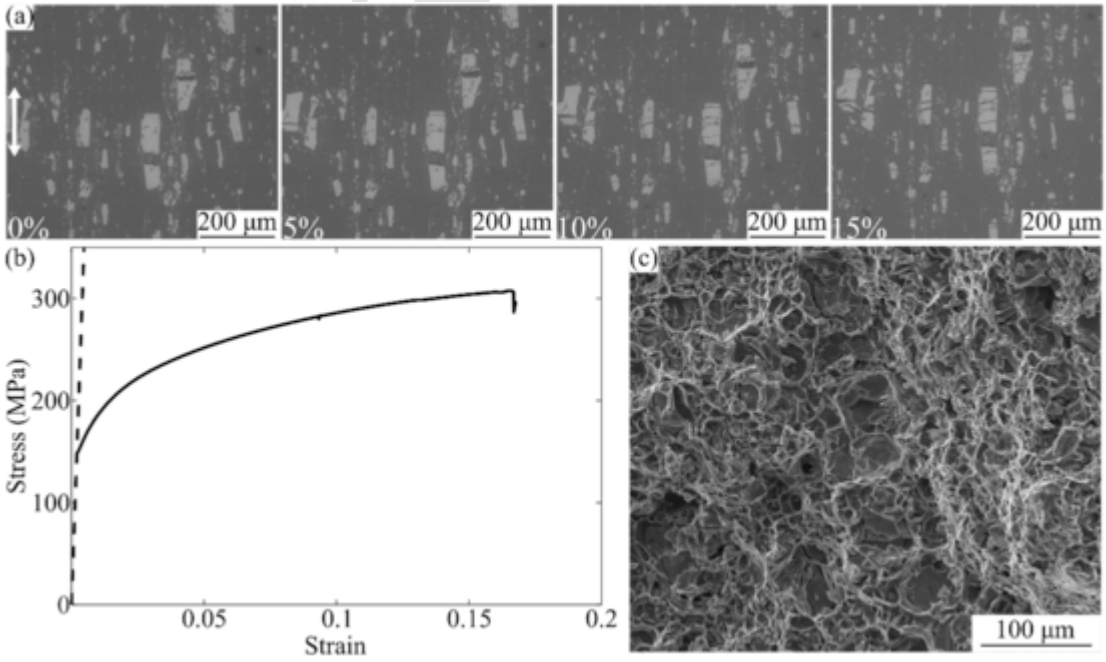

Fig. 4. (a) SEM backscatter images at different strain points during in-situ tensile testing of Al-8Ce-10Mg 52:1. (b) The stress-strain data from in-situ tensile testing. (c) SEM secondary image of fracture surface after in-situ tensile testing indicating ductile fracture.

CORRECTED PROOF

more microcracks occur, the matrix reaches a critical stress point 304 MPa and failure occurs rapidly, as shown in Fig. 4(b).

The SEM images captured during tensile testing were used to calculate the strain at which individual intermetallic phases first formed microcracks. The strain at which microcracking occurred was calculated by manual measurement of the length of the multiple intermetallics in the reference image and the image right before each intermetallic cracked. The average strain calculated for initial cracking of 11 intermetallics was 0.71% ± 0.16%. The data from in-situ testing supports a linear elastic fracture response for the intermetallics, which agrees with results from a similar study for Al-Cu intermetallics [19], and is consistent with the fracture behavior of complex intermetallic phases.

Using data obtained from nanoindentation of an Al-Ce intermetallic, the Young's modulus was calculated to be 110.8 GPa using Eq. (8). This value was almost 50% larger than the Al(Mg) grains at 74.46 GPa [36, 42]. Using the 1-dimensional Hooke's law equation, $\sigma = E\varepsilon$, the stress at fracture was calculated to be 787 MPa for the intermetallic.

In-situ SEM-DIC tensile testing was performed to observe the strain distribution in the two different phases. An area with a sufficient pattern density with a large Al-Ce intermetallic surrounded by Al(Mg) grains was imaged during loading. Images were captured before and after a lateral crack occurred in the large Al-Ce intermetallic, and the backscatter images and DIC strain results (in the direction of loading, ε_{yy}) are shown in Fig. 5.

The DIC results prior to cracking (Fig. 5(a)), show that the average strain in the intermetallic was 0.0015 μm/μm with a maximum of 0.0035 μm/μm in the region where cracking occurred. Furthermore, the average strain in the surrounding Al(Mg) was 0.015 μm/μm. There was an order of magnitude difference in strain between the intermetallic and grains. The grains are in a state of high strain while the intermetallics are in a state of high stress. After the intermetallic fracture, the average strain in the matrix increased to 0.035 μm/μm (see Fig. 5 (b)). The localized stress by the grains on the intermetallic caused a crack and allowed for the plastic deformation to continue in the grains. The load sharing effect observed in this study is consistent with the load sharing effect observed for the neutron diffraction measurements done on Al-Ce alloys undergoing compressive loading [4], and it ultimately leads to microcrack nucleation in the intermetallic phase.

3.4. Calibration of CPFEM via optimization for Al-10Mg-8Ce

There are six material constants required to describe the mechanical behavior in the crystal plasticity framework. The first three are single crystal elastic constants C_{11}, C_{12}, and C_{44}, which were calculated using the nanoindentation data. The other three are plastic constants h_o, τ_s, and τ_o. Each plastic constant affects the bulk material response of a polycrystalline material differently. The initial hardening modulus, h_o, affects the slope of the initial plastic region of the bulk material's stress-strain curve while the initial stress, τ_o, affects the bulk materials yield stress. Additionally, the saturation stress, τ_s, affects the slope of the plastic region at larger strains of the bulk material's stress-strain curve [43]. The constants of an alloy are commonly calibrated by using tensile stress versus strain data [27,43–45]. While trial and error can be used to try and fit the simulated data to the experimental data, studies have employed optimization techniques such as the Newton–Raphson Method to improve accuracy and reduce the computation time [46].

For calibrating the parameters used in this work, a Representative Volume Element (RVE) with Voronoi tessellation was created using Neper software [47], in combination with an optimization scheme to calibrate the RVE's stress-strain curve to experimental data. The tessellation dimensions were 0.2 × 0.2 × 0.01 mm, as shown in Fig. 6(a). The data from EBSD were used to create both phases of the microstructure with accurate size and texture orientations. The Al-Ce intermetallics correspond to the black regions, while the Al(Mg) grains are displayed as multicolored sets in Fig. 6(a).

A dynamic implicit quasi static Abaqus simulation was used. The boundary conditions for the model were simple tension similar to the experimental in-situ tension test and a strain of 15% was applied. Additionally, there was a total of 28,224 quadrilateral C3D8R elements in the model. Crystal plasticity was given to the Al(Mg) grains, whereas the Al-Ce intermetallics were given a linear elastic fracture response using the ductile damage option. The fracture stress of the intermetallic was set to 787 MPa with a Young's modulus of 110.8 GPa calculated using results from in-situ testing in Section 3.3.

A Python script was written for the calibration of the model using a modified iterative Newton–Raphson algorithm developed by Guery et al. [46]. Each iterative step starts with a set of values for $[h_o, \tau_s, \tau_o]$ and

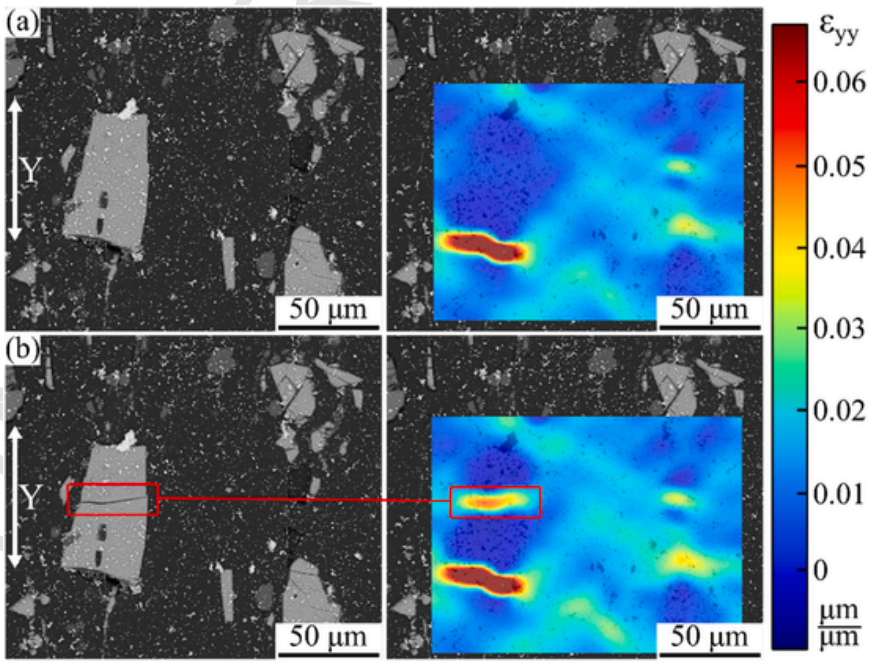

Fig. 5. Backscatter SEM images and overlaid strain distribution maps (a) just before a crack formed in the Al-Ce intermetallic and (b) just after the formation of the crack.

UNCORRECTED PROOF

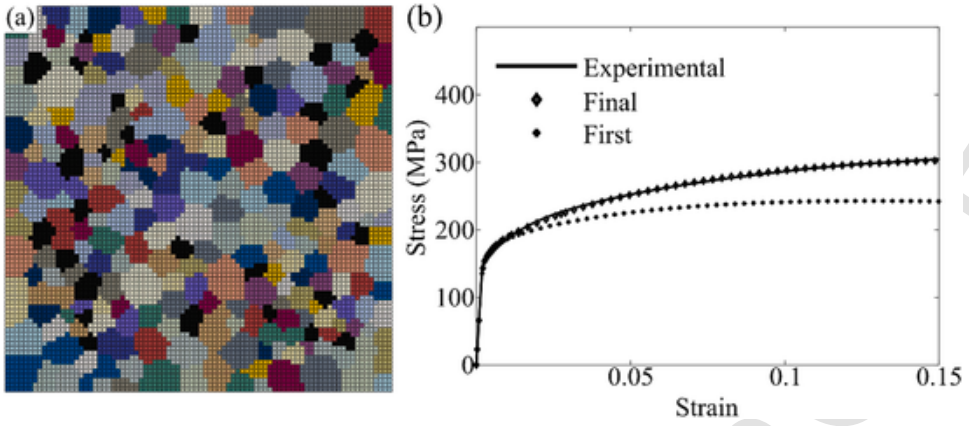

Fig. 6. (a) Voronoi tessellation for calibration of the CPFEM plastic parameters. The black areas represent the Al-Ce intermetallics. (b) Plotted comparison of the stress-strain curves of the first iteration, and the final iteration matching the experimental data.

four simulations are run. The first simulation determines the total error between the experimental and simulated data. The difference in the stress values at 775 strain points is calculated between the experimental and simulated data. The value for the total error is calculated using Eq. (17) where Z is the total error, N_t is the number of strain points, and the vector $\{\delta F\}$ is the difference in stress values of the experimental and simulated strain values. A dot product of the $\{\delta F\}$ vector is evaluated, resulting in a positive scalar quantity for the total error:

$$Z = \frac{1}{2N_t}\{\delta F\}^T\{\delta F\} \tag{17}$$

The iterative process stops when the total error reaches a user defined minimum. The next three simulations consist of the same set of $[h_o, \tau_s, \tau_o]$, but for each simulation either h_o,τ_s, or $\tau_o$is changed by a set value Δx. For example, the second and third simulations will use the sets $[h_o + \Delta x, \tau_s, \tau_o]$ and $[h_o, \tau_s + \Delta x, \tau_o]$, respectively. The stress-strain data is taken from each of these simulations to determine the sensitivity of the total error due to a small change in each parameter. The sensitivity is calculated from the Hessian tensors in Eqs. (18) and (19). The variable, n, is the iteration step and the matrix, $[S_F]$, is the sensitivity matrix from the change in each parameter. The matrix, $[H_F]$, is defined as:

$$\left[H_F^{(n-1)}\right] = \frac{1}{N_t}\left[S_F^{(n-1)}\right]^T\left[S_F^{(n-1)}\right] \tag{18}$$

While the vector, $\{h_F\}$, is the product of the sensitivity matrix and difference in load, as taken from the first simulation for the nth iteration:

$$\left\{h_F^{(n-1)}\right\} = \frac{1}{N_t}\left[S_F^{(n-1)}\right]^T\{\delta F\} \tag{19}$$

The Hessian tensors are used in Eq. (20) to determine the necessary change in each of the parameters $\{p\}$. The process is repeated with a new set of parameters $\{p\} + \{\delta p\}$:

$$\left[H_F^{(n-1)}\right]\{\delta p^{(n)}\} = \left\{h_F^{(n-1)}\right\} \tag{20}$$

The python script was started using an initial set of parameters, $[h_o, \tau_s, \tau_o]$, as determined for a 5000 series Al model [48]. The script used a total of 25 iterations for the total error to reach a user defined minimum of 0.001 (with Δx set to 3). The final set of values for $[h_o, \tau_s, \tau_o]$ are displayed in Table 2. Fig. 6(b) shows the change in the error between the stress-strain curves for the simulated and experimental results, as determined from the first to the final set of values. The final set of values gives computational results that are in good agreement with the experimental stress-strain data.

Table 2
Final set of calibrated crystal plasticity values for the Al-8Ce-10Mg alloy model.

h_o (MPa)	τ_s (MPa)	τ_o (MPa)
118.1	83.61	39.41

3.5. The effect of area percent of Al-Ce intermetallic in the bulk

In this section, the calibrated model was utilized to study the effect of area percentage of Al-Ce intermetallic in the bulk material. Analysis of the EBSD data showed that the average area percentage of intermetallic is around 10% in this alloy. In-situ testing revealed that the intermetallics have a high strength, but their brittle nature leads to the formation of microcracks. It was hypothesized that if an increase in the intermetallic content occurs, the strength will improve but at a cost of ductility in the bulk material, where failure occurs due to an earlier coalescence of microcracks.

To investigate this hypothesis, two tessellations were created, one with 10% intermetallics and the other with 20% intermetallics, as shown in Fig. 7(a) and (b). The models had the same dimensions as the optimization model, 0.2 × 0.2 × 0.01 mm with 28,224 quadrilateral C3D8R elements. The crystal plasticity parameters in Table 2 were used for the Al(Mg) grains and a linear elastic fracture response was used for the Al-Ce intermetallics. Simple tension boundary conditions were applied, and the simulations were run until significant damaged occurred in the model.

The stress-strain curves, as displayed in Fig. 7(c), show that the slope of the initial plastic region increased with an increase in the intermetallic area. However, failure occurs at 60% of the total strain with the higher percentage of intermetallics. Simulations reveal that an increase in the area percentage of intermetallics will lead to more microcracking in the microstructure. This increase in the amount of microcracking compromises the ductility of alloy, leading to failure at lower strain. Studies which investigated the effect of weight percentage of Ce (between 5% and 12%) on the mechanical behavior of Al-Ce alloys, concluded that an increase in Ce weight percent directly decreases the tensile ductility of the alloy. These results agree with the prediction of our simulations on Al-8Ce-10Mg [4,7].

3.6. The effect of microstructural texture on the yield strength

Texture is one of the microstructural features that can be tailored by standard post-processing methods. If the effect of texture on the me-

UNCORRECTED PROOF

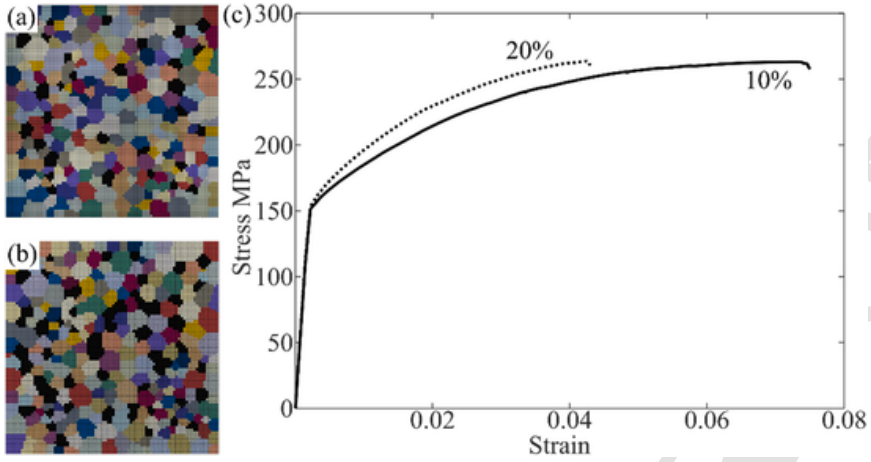

Fig. 7. Voronoi tessellation of the Al-8Ce-10Mg alloy with the (a) 10% and (b) 20% Al-Ce intermetallic by area. (c) Comparison of stress-strain curves showing the effect of intermetallic area percent.

chanical properties is known, it can be tailored to control the mechanical behavior to a given application. In this section, we utilize the calibrated CPFEM model to investigate the link between the texture, yield strength, and microcracking damage of this two-phase alloy. In the extruded alloy, the material has a slight [110] texture along the extrusion/loading direction (Fig. 2(b)). To examine the effect of other possible textures on the overall bulk material's strength, three cases were also explored: (*i*) the [110] texture measured by the EBSD, (*ii*) perfect [111] texture, and (*iii*) [111] texture with a 10° standard deviation along the loading direction. The crystal plasticity material properties were kept the same for the Al(Mg) grains, as well as the linear elastic fracture behavior for the Al-Ce intermetallic. In-situ tensile testing data revealed an apparent strong interfacial bond between the two main phases, consistent with the literature [4], and was assumed in these simulations. Simulation results are reported at 1% strain to investigate the effect of texture on the yield strength and microcracking initiation in the intermetallics. The inverse pole figures for both [111] texture cases are shown in Fig. 8(a), where a clear [111] texture is shown in the loading direction.

An improvement was made by aligning the grains in the [111] direction and requiring more bulk force to cause damage in the intermetallic phase. Fig. 8(b) shows an area of the model with intermetallics, outlined in black, surrounded by grains, outlined in gray, for the texture cases of the [110] and perfect [111] with loading in the Z direction. More microcracking damage occurred in the [110] texture than the [111] texture. Moreover, the [111] texture has both a uniform and higher stress state in the microstructure than the [110] texture. This result suggests that less microcracking damage occurred in the material and that there was a continuation of its load carrying capability. A comparison of the stress-strain curves for each [111] texture case (Fig. 8(c)) shows an improvement in the yield strength over the [110] case. By aligning the microstructural texture in the [111] direction perfectly, an improvement of 48.6% for the yield stress (as compared to the [110] texture) was achieved. For the case of 10% standard deviation along the [111] direction, an improvement of 25.0% for the yield strength was also observed.

Analysis of the DIC data showed that before a microcrack occurred in the intermetallic, the strain in the Al(Mg) grains is higher than that of the intermetallic and the results of the simulations agree with the experimental DIC results in Section 3.3. The stress is localizing near the grain/intermetallic interface to cause damage by microcrack initiation in the intermetallic to relieve stress so that the material can continue to plastically deform. It is well known that in FCC metals, by having a texture in which the [111] directions are aligned with the loading, a larger force is needed to reach the resolved shear stress and activate the plastic deformation by crystalline slip. This phenomenon has been shown in experiments on many FCC metals, including Cu and Ag [49–52]. As discussed earlier, the microcracking in the intermetallics is directly governed by the plastic deformation in the matrix, and having the texture will delay the failure in the material. With that being said, our compu-

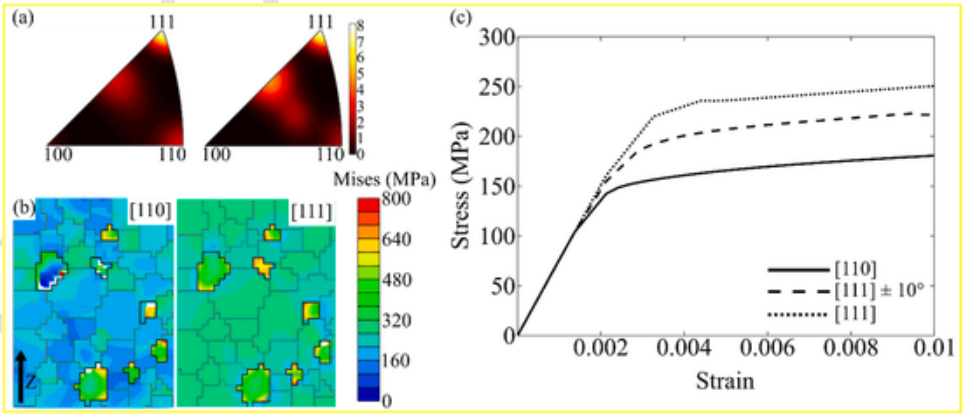

Fig. 8. (a) (Left) The inverse pole figure of the model with a [111] texture, and (right) with a [111] texture given a 10° standard deviation. (b) (Left) Tensile simulation results for the mises stress in the microstructure of [110] texture, and (right) simulation results for the mises stress in the microstructure of perfect [111] texture at 1% strain. The Al-Ce intermetallic is outlined in black and the Al(Mg) grains are outlined in gray. The loading direction was on the Z-axis, indicated by the black arrow. (c) Comparison of the stress-strain curves for three textures.

tational results in this section are compatible with the theoretical and experimental expectations.

4. Conclusions

A crystal plasticity finite element model was developed for the extruded Al-8Ce-10Mg alloy. The material constants required for modeling this alloy were calculated and calibrated using a set of experimental measurements including SEM/EBSD imaging, nanoindentation, and in-situ SEM tensile testing. A computational framework was then utilized to minimize the error between the computational and experimental results. Our in-situ tensile tests revealed that the failure of the alloy occurred due to the coalescence of microvoids. The computational results show that an increase in the area percentage of intermetallic increased the initial slope of plastic region but sacrificed some ductility of the material. The results also indicate that the texture of the alloy greatly affected the yield strength of the alloy. Simulation results showed that a maximum of 48.6% improvement of the yield strength can be achieved by having a microstructural texture in the [111] direction, and more applied force would be required to cause cracking in the intermetallic phase. Lastly, the developed CPFEM model and the determined properties can be used to expand the model's capabilities with future validation efforts for Al-Ce alloys.

CRediT authorship contribution statement

Ryan J. Lane: Conceptualization, Methodology, Software, Validation, Investigation, Writing – original draft, Writing – review & editing. **Ayyoub M. Momen:** Conceptualization, Writing – review & editing. **Michael S. Kesler:** Conceptualization, Methodology, Writing – review & editing. **Jamieson Brechtl:** Conceptualization, Writing – review & editing. **Orlando Rios:** Conceptualization, Methodology, Writing – review & editing. **Kashif Nawaz:** Conceptualization, Methodology, Writing – review & editing. **Reza Mirzaeifar:** Conceptualization, Resources, Supervision, Writing – review & editing, Project administration, Funding acquisition.

Declaration of Competing Interest

The authors declare that they have no known competing financial interests or personal relationships that could have appeared to influence the work reported in this paper.

Acknowledgments

This work was sponsored by the U.S. Department of Energy Building Technologies Office under Contract No. BENEFIT 1632_1520 and NFE-17-06541 with UT-Battelle, LLC. We would also like to thank the Critical Materials Institute, an Energy Innovation Hub funded by the U.S. Department of Energy, and Eck Industries for providing material samples.

References

[1] T. Fishman, R. Myers, O. Rios, T.E. Graedel, Implications of emerging vehicle technologies on rare earth supply and demand in the United States, Resources 7 (1) (2018) 9.
[2] S.M. Fortier, et al., Draft Critical Mineral List—Summary of Methodology and Background Information—U.S. Geological Survey Technical Input Document in Response to Secretarial Order No. 3359, Open-File Report, Reston, VA, 2018, p. 26.
[3] Directorate-General for Communications Networks, C.a.T.E.C., European Commission, Communication from the Commission to the European Parliament, the Council, the European Economic and Social Committee and the Committee of the Regions, 2020.
[4] Z.C. Sims, O.R. Rios, D. Weiss, P.E.A. Turchi, A. Perron, J.R.I. Lee, T.T. Li, J.A. Hammons, M. Bagge-Hansen, T.M. Willey, K. An, Y. Chen, A.H. King, S.K. McCall, High performance aluminum–cerium alloys for high-temperature applications, Mater. Horiz. 4 (6) (2017) 1070–1078.
[5] D. Weiss, Castability and Characteristics of High Cerium Aluminum Alloys, 2018.
[6] Z.C. Sims, D. Weiss, S.K. McCall, M.A. McGuire, R.T. Ott, T. Geer, O. Rios, P.A.E. Turchi, Cerium-based, intermetallic-strengthened aluminum casting alloy: high-volume co-product development, JOM 68 (7) (2016) 1940–1947.
[7] D. Weiss, Improved high-temperature aluminum alloys containing cerium, J. Mater. Eng. Perform. 28 (4) (2019) 1903–1908.
[8] Ø. Ryen, B. Holmedal, O. Nijs, E. Nes, E. Sjölander, H.E. Ekström, Strengthening mechanisms in solid solution aluminum alloys, Metall. Mater. Trans. A 37 (6) (2006) 1999–2006.
[9] H.B. Henderson, et al., Ternary interactions and implications for third element alloying potency in Al–Ce-based alloys, Light Metals 2020, Springer International Publishing, Cham, 2020.
[10] E.T. Stromme, H.B. Henderson, Z.C. Sims, M.S. Kesler, D. Weiss, R.T. Ott, F. Meng, S. Kassoumeh, J. Evangelista, G. Begley, O. Rios, Ageless aluminum-cerium-based alloys in high-volume die casting for improved energy efficiency, JOM 70 (6) (2018) 866–871.
[11] F. Czerwinski, Cerium in aluminum alloys, J. Mater. Sci. 55 (1) (2020) 24–72.
[12] M.S. Kesler, M.L. Neveau, W.G. Carter, H.B. Henderson, Z.C. Sims, D. Weiss, T.T. Li, S.K. McCall, M.E. Glicksman, O. Rios, Liquid direct reactive interface printing of structural aluminum alloys, Appl. Mater. Today 13 (2018) 339–343.
[13] Y. Liu, R.A. Michi, D.C. Dunand, Cast near-eutectic Al-12.5 wt% Ce alloy with high coarsening and creep resistance, Mater. Sci. Eng. A 767 (2019) 138440.
[14] F. Czerwinski, B. Shalchi, On the Al–Al11Ce3 eutectic transformation in aluminum–cerium binary alloys, Materials 13 (20) (2020) 4549.
[15] F. Roters, P. Eisenlohr, T.R. Bieler, D. Raabe, Crystal plasticity finite element methods, Materials Science and Engineering, Crystal Plasticity Finite Element Methods, 2010.
[16] C.C. Tasan, M. Diehl, D. Yan, C. Zambaldi, P. Shanthraj, F. Roters, D. Raabe, Integrated experimental–simulation analysis of stress and strain partitioning in multiphase alloys, Acta Mater. 81 (2014) 386–400.
[17] T. Park, L.G. Hector, X. Hu, F. Abu-Farha, M.R. Fellinger, H. Kim, R. Esmaeilpour, F. Pourboghrat, Crystal plasticity modeling of 3rd generation multi-phase AHSS with martensitic transformation, Int. J. Plast. 120 (2019) 1–46.
[18] B. Mohammed, et al., Multiscale crystal plasticity modeling of multiphase advanced high strength steel, Int. J. Solids Struct. (2017).
[19] S. Bahl, X. Hu, E. Hoar, J. Cheng, J.A. Haynes, A. Shyam, Effect of copper content on the tensile elongation of Al–Cu–Mn–Zr alloys: experiments and finite element simulations, Mater. Sci. Eng. A 772 (2020) 138801.
[20] Y. Huang, A User-Material Subroutine Incroporating Single Crystal Plasticity in the ABAQUS Finite Element Program, Harvard University, 1991.
[21] F. Roters, M. Diehl, P. Shanthraj, P. Eisenlohr, C. Reuber, S.L. Wong, T. Maiti, A. Ebrahimi, T. Hochrainer, H.O. Fabritius, S. Nikolov, M. Friák, N. Fujita, N. Grilli, K. G.F. Janssens, N. Jia, P.J.J. Kok, D. Ma, F. Meier, E. Werner, M. Stricker, D. Weygand, D. Raabe, DAMASK – the Düsseldorf advanced material simulation kit for modeling multi-physics crystal plasticity, thermal, and damage phenomena from the single crystal up to the component scale, Comput. Mater. Sci. 158 (2019) 420–478.
[22] G.I. Taylor, Plastic strain in metals, J. Inst. Met. 62 (1938) 307–324.
[23] J.R. Rice, Inelastic constitutive relations for solids: an internal-variable theory and its application to metal plasticity, J. Mech. Phys. Solids 19 (6) (1971) 433–455.
[24] R. Hill, Generalized constitutive relations for incremental deformation of metal crystals by multislip, J. Mech. Phys. Solids 14 (2) (1966) 95–102.
[25] R.J. Asaro, Micromechanics of crystals and polycrystals, in: J.W. Hutchinson, T.Y. Wu (Eds.), Advances in Applied Mechanics, Elsevier, 1983, pp. 1–115.
[26] D. Peirce, R.J. Asaro, A. Needleman, An analysis of nonuniform and localized deformation in ductile single crystals, Acta Metall. 30 (6) (1982) 1087–1119.
[27] M. Ghodrati, M. Ahmadian, R. Mirzaeifar, Three-dimensional study of rolling contact fatigue using crystal plasticity and cohesive zone method, Int. J. Fatigue 128 (2019) 105208.
[28] M.A. Groeber, M.A. Jackson, DREAM.3D: a digital representation environment for the analysis of microstructure in 3D, Integr. Mater. Manuf. Innov. 3 (1) (2014) 56–72.
[29] D. Weiss, Composites and Alloys Based on the Al-Ce System, 2019.
[30] A.D. Kammers, University of Michigan Library, Deep Blue, The Influence of Microstructure on the Deformation and Failure of Ultrafine-Grained Aluminum, 2014.
[31] M.A. Linne, A. Venkataraman, M.D. Sangid, S. Daly, Grain boundary sliding and slip transmission in high purity aluminum, Exp. Mech. 59 (5) (2019) 643–658.
[32] J. Blaber, B. Adair, A. Antoniou, Ncorr: open-source 2D digital image correlation matlab software, Exp. Mech. 55 (6) (2015) 1105–1122.
[33] D.T. Pierce, K. Nowag, A. Montagne, J.A. Jiménez, J.E. Wittig, R. Ghisleni, Single crystal elastic constants of high-manganese transformation- and twinning-induced plasticity steels determined by a new method utilizing nanoindentation, Mater. Sci. Eng. A 578 (2013) 134–139.
[34] J.J. Vlassak, W.D. Nix, Measuring the elastic properties of anisotropic materials by means of indentation experiments, J. Mech. Phys. Solids 42 (8) (1994) 1223–1245.
[35] M. Levy, H. Bass, R. Stern, Handbook of Elastic Properties of Solids, Liquids, and Gases, Four-Volume Set, Academic Press, 2000.
[36] W.C. Oliver, G.M. Pharr, An improved technique for determining hardness and elastic modulus using load and displacement sensing indentation experiments, J. Mater. Res. 7 (6) (1992) 1564–1583.
[37] J.J. Vlassak, W.D. Nix, Indentation modulus of elastically anisotropic half spaces, Philos. Mag. A 67 (5) (1993) 1045–1056.
[38] H.M. Ledbetter, Monocrystal-polycrystal elastic constants of a stainless steel, Phys. Status Solidi (a) 85 (1) (1984) 89–96.
[39] W. Ebhota, T.-C. Jen, Intermetallics Formation and Their Effect on Mechanical Properties of Al-Si-X Alloys, 2018.
[40] S.S. Singh, E. Guo, H. Xie, N. Chawla, Mechanical properties of intermetallic

UNCORRECTED PROOF

inclusions in Al 7075 alloys by micropillar compression, Intermetallics 62 (2015) 69–75.
[41] J. Mathew, G. Remy, M.A. Williams, F. Tang, P. Srirangam, Effect of Fe intermetallics on microstructure and properties of Al-7Si alloys, JOM 71 (12) (2019) 4362–4369.
[42] G.M. Pharr, W.C. Oliver, F.R. Brotzen, On the generality of the relationship among contact stiffness, contact area, and elastic modulus during indentation, J. Mater. Res. 7 (1992) 613–617.
[43] I. Simonovski, K.-F. Nilsson, L. Cizelj, Material Properties Calibratian for 316L Steel Using Polycrystalline Model, 2005.
[44] K. Sedighiani, M. Diehl, K. Traka, F. Roters, J. Sietsma, D. Raabe, An efficient and robust approach to determine material parameters of crystal plasticity constitutive laws from macro-scale stress–strain curves, Int. J. Plast. 134 (2020) 102779.
[45] S. El Shawish, L. Cizelj, Combining single- and poly-crystalline measurements for identification of crystal plasticity parameters: application to austenitic stainless steel, Crystals 7 (2017) 181.
[46] A. Guery, F. Hild, F. Latourte, S. Roux, Identification of crystal plasticity parameters using DIC measurements and weighted FEMU, Mech. Mater. 100 (2016) 55–71.
[47] R. Quey, P.R. Dawson, F. Barbe, Large-scale 3D random polycrystals for the finite element method: generation, meshing and remeshing, Comput. Methods Appl. Mech. Eng. 200 (17) (2011) 1729–1745.
[48] C. Pinna, Y. Lan, M.F. Kiu, P. Efthymiadis, M. Lopez-Pedrosa, D. Farrugia, Assessment of crystal plasticity finite element simulations of the hot deformation of metals from local strain and orientation measurements, Int. J. Plast. 73 (2015) 24–38.
[49] X. Zhang, H. Wang, X.H. Chen, L. Lu, K. Lu, R.G. Hoagland, A. Misra, High-strength sputter-deposited Cu foils with preferred orientation of nanoscale growth twins, Appl. Phys. Lett. 88 (17) (2006) 173116.
[50] R.T. Ott, J. Geng, M.F. Besser, M.J. Kramer, Y.M. Wang, E.S. Park, R. LeSar, A.H. King, Optimization of strength and ductility in nanotwinned ultra-fine grained Ag: twin density and grain orientations, Acta Mater. 96 (2015) 378–389.
[51] R. Yuan, I.J. Beyerlein, C. Zhou, Coupled crystal orientation-size effects on the strength of nano crystals, Sci. Rep. 6 (1) (2016) 26254.
[52] Y.-J. Li, K.-N. Tu, C. Chen, Tensile properties of <111>-oriented nanotwinned Cu with different columnar grain structures, Materials 13 (6) (2020) 1310.

UNCORRECTED PROOF